Analysis of semi-empirical interatomic potentials appropriate for simulation of crystalline and liquid Al and Cu

M.I. Mendelev, M.J. Kramer, C.A. Becker & M. Asta

Taylor & Francis
Taylor & Francis Group

Analysis of semi-empirical interatomic potentials appropriate for simulation of crystalline and liquid Al and Cu

M.I. Mendelev[a]*, M.J. Kramer[a], C.A. Becker[b] and M. Asta[c]

[a]*Materials and Engineering Physics, Ames Laboratory, Ames, IA 50011, USA;*
[b]*Metallurgy Division, National Institute of Standards and Technology, Gaithersburg, MD 20899, USA;* [c]*Department of Chemical Engineering and Materials Science, University of California, Davis, CA 95616, USA*

We investigate the application of embedded atom method (EAM) interatomic potentials in the study of crystallization kinetics from deeply undercooled melts, focusing on the fcc metals Al and Cu. For this application, it is important that the EAM potential accurately reproduces melting properties and liquid structure, in addition to the crystalline properties most commonly fit in its development. To test the accuracy of previously published EAM potentials and to guide the development of new potential in this work, first-principles calculations have been performed and new experimental measurements of the Al and Cu liquid structure factors have been undertaken by X-ray diffraction. We demonstrate that the previously published EAM potentials predict a liquid structure that is too strongly ordered relative to measured diffraction data. We develop new EAM potentials for Al and Cu to improve the agreement with the first-principles and measured liquid diffraction data. Furthermore, we calculate liquid-phase diffusivities and find that this quantity correlates well with the liquid structure. Finally, we perform molecular dynamics simulations of crystal nucleation from the melt during quenching at constant cooling rate. We find that EAM potentials, which predict the same zero-temperature crystal properties but different liquid structures, can lead to quite different crystallization kinetics. More interestingly, we find that two potentials predicting very similar equilibrium solid and liquid properties can still produce very different crystallization kinetics under far-from-equilibrium conditions characteristic of the rapid quenching simulations employed here.

Keywords: *ab initio*; diffraction methods; diffusion; interatomic potential; liquid metals; molecular dynamic simulations; solidification

1. Introduction

Atomistic simulations have been used extensively over the past decade as a framework for investigating solidification phenomena in metals and alloys. To date, most of this simulation work has been devoted to the calculation of the thermodynamic [1–8] and kinetic [5,9–13] properties of crystal–melt interfaces as a framework for predictive modelling of solidification growth rates and related microstructural morphologies.

*Corresponding author. Email: mendelev@ameslab.gov

More recently, atomistic simulations have been applied in detailed investigations of nucleation kinetics [14–19]. This work includes the first recent calculations of the absolute rates of homogeneous nucleation from a highly undercooled metallic melt [20]. There is clear interest in extending such studies to multicomponent alloys, where simulations can be used to investigate a number of issues related to glass formation and related phenomena. A prerequisite to performing such simulations for specific alloy systems is the need to understand the extent to which simulated nucleation kinetics in elemental systems are influenced by the details of the underlying interatomic potentials. Quantitative studies of nucleation rates require accurate predictions of diffusion rates, bulk and interfacial thermodynamic properties in highly undercooled melts. However, no systematic exploration has been undertaken to investigate the extent to which these properties depend on the details of the interatomic potential underlying a classical atomistic simulation.

The most widely used semi-empirical model for describing interatomic interactions in metals and alloys is the embedded atom method (EAM) [21,22]. The total energy in this method is divided into two contributions: a pairwise part and a local density part:

$$U = \sum_{i=1}^{N-1} \sum_{j=i+1}^{N} \varphi(r_{ij}) + \sum_{i=1}^{N} \Phi(\rho_i) \tag{1}$$

where the subscripts i and j label distinct atoms, N is the number of atoms in the system, $r_{i,j}$ is the separation between atoms i and j, φ is the pair potential contribution to the cohesive energy and Φ represents the energy to embed an atom in a background charge density, ρ_i:

$$\rho_i = \sum_{j} \psi(r_{ij}) \tag{2}$$

where ψ is the contribution from neighbouring atom j. Thus, three functions, $\varphi(r)$, $\psi(r)$ and $\Phi(\rho)$, should be known to define an EAM potential model for a single component system.

In the earliest applications of the EAM (see, for example, [23–25]), these potential functions were fit to room-temperature crystal properties. With such a set of input data, it is clearly not guaranteed that the potential will properly predict finite-temperature properties, such as the melting temperature (T_m). Indeed, it has been found that EAM-calculated values of T_m can differ substantially from the experimentally measured value, by as much as 500 K (see, for example, [26]). Such errors are a serious problem for applications of EAM potentials to quantitative studies of crystallization phenomena. Recently, Sturgeon and Laird [27] proposed a simple way to fix this problem and now EAM potentials providing accurate melting temperatures can be developed readily. It should be noted that correct reproduction of other melting point data (change in volume and latent heat) are also very important requirements of a potential for accurate prediction of nucleation rates and crystal-melt interface properties. For example, the analysis of simulation data for fcc and bcc metals supports Turnbull's observation that the magnitude of the crystal–melt interfacial free energy in metals scales with the magnitude of the latent heat (see, for example, [12]).

It is also known that the liquid diffusion coefficient in metals depends strongly on liquid structure and density. Similarly, recent calculations of crystal–melt interfacial free energies in Al [28] suggest that the crystal–melt interfacial free energy is larger in systems

with more highly ordered melt structures. An interatomic potential suitable for the simulation of crystallization kinetics should, thus, be able to properly reproduce the liquid structure. A basis for comparing liquid structure predictions with experiment can be made at the level of the structure factor, obtained from diffraction measurements (see, for example, [29]). From the Fourier transformation of the measured structure factor, one can compute the radial distribution function, $g(r)$, referred to below as the pair correlation function (PCF):

$$g(r) = 1 + \frac{V}{2\pi^2 N} \int_0^\infty [S(Q) - 1] \frac{\sin Qr}{Qr} Q^2 \, dQ. \tag{3}$$

The PCF can be directly calculated in a straightforward manner from molecular dynamics (MD) simulations.

Since semi-empirical potentials are usually developed without account of liquid structure data, there is no reason *a priori* to expect that they will provide good agreement with experimental data. Even by using the so-called force matching method, where the atomic forces obtained from first-principles calculations for a representative liquid configuration are used in the fitting database of a potential [26,30], accurate liquid structure predictions cannot be guaranteed (see below). Thus, it is possible to obtain two semi-empirical potentials for the same metal that will predict similar crystal properties but different liquid structures. In this case, there is no reason to expect that these potentials will lead to similar results in the simulation of crystallization kinetics. Indeed, several Al potentials were considered by Morris et al. [28]. While they all predict similar low-temperature crystal properties and even melting temperatures, they lead to different liquid structures. These potentials were also found to predict significantly different values for the crystal–melt interfacial free energies. A related observation is that the Al potential leading to the largest value of this interfacial free energy. The most ordered liquid structure (namely the one proposed by Ercolessi and Adams [30], and referred to below as the EA potential), gives rise to sufficiently low nucleation rates such that crystallization was not observable in deeply undercooled melts on the time scale of MD simulations [31]. On the other hand, the potential described in [32] (referred below as MSAHM potential) readily crystallized in simulations at very large supercooling [20].

In the present work, we investigate in further detail the application of EAM models in the study of liquid and melting properties and crystallization kinetics, focusing on two fcc metals: Al and Cu. For each of these metals, we prepare a set of target bulk solid properties, taken either from experiment or from first-principles calculations. We consider two EAM potentials for Al and Cu from the literature that provide reasonable melting-point predictions. Using these potentials, we calculate bulk liquid and solid properties, and compare them with target values to ascertain areas where the potentials can be further improved. Consequently, we develop three new EAM potentials that provide better agreement with the target bulk properties. Next, the liquid diffusivities are determined for each of these potentials and we find that these values indeed depend on the details of the potential model in a manner than can be explained via the predicted liquid structure factor. Finally, MD simulations of crystallization kinetics in undercooled liquids are performed for each of the potentials. In some cases, these simulations lead to unanticipated results. We discuss these results at the end of the paper and summarize the relevance of these findings for studies of crystallization kinetics in metals and alloys.

2. Target properties

2.1. *Target properties*

Tables 1 and 2 contain lists of the target properties used to test the accuracy of previously published EAM potentials and to fit new interatomic potential models in the present work. Most of the properties listed in these tables are taken from the literature; the methods used to determine the remaining properties from first-principles calculations and experimental measurements will be described below. In this section, we briefly review our choice of target properties.

A potential suitable for the simulation of crystallization kinetics should properly describe bulk solid and liquid structural, elastic and thermodynamic properties, as well as melting properties. Tables 1 and 2 contain a number of such target properties, including cohesive energy, lattice parameters and elastic moduli of the stable fcc phase, melting temperature, latent heat, volume change on melting, and liquid density. Since both Cu and

Table 1. Bulk properties of Al: target values and values calculated with EAM potentials.[1]

Property	Target value	EA	MSAHM	Al1	Al2
a (fcc) (Å)	4.032 [62]	**4.032**	**4.033**	4.045	4.045
E_{coh} (fcc) (eV/atom)	−3.362 [63]	**−3.360**	**−3.370**	−3.411	−3.466
C_{11} (GPa)	118 [64]	**118**	117	110	112
C_{12} (GPa)	62 [64]	**62**	62	61	62
C_{44} (GPa)	33 [64]	37	33	33	37
E_f^v (unrelaxed fcc) (eV/atom)	0.66 [62]	**0.78**	**0.69**	0.68	0.72
E_f^v (relaxed fcc) (eV/atom)		0.69	0.68	0.66	0.69
E_f^i ($\langle 100 \rangle$ fcc) (eV/atom)	2.43 [65]	**2.46**	**2.42**	2.33	2.39
A (bcc) (Å)	3.229 [62]	**3.148**	**3.219**	3.238	3.237
$\Delta E_{fcc \rightarrow bcc}$ (eV/atom)	0.100 [62]	**0.057**	**0.074**	0.102	0.102
a (hcp) (Å)	2.847 [62]	**2.817**	**2.844**	2.845	2.845
c (hcp) (Å)	4.714 [62]	**4.880**	**4.721**	4.746	4.748
$\Delta E_{fcc \rightarrow hcp}$ (eV/atom)	0.028 [62]	**0.018**	**0.028**	0.028	0.028
γ_{100} (fcc at $T=0$) (meV/Å^2)	84.1 [69]	**59.6**	12.3	31.0	33.4
γ_{110} (fcc at $T=0$) (meV/Å^2)	79.3 [69]	**65.2**	20.5	36.3	37.9
γ_{111} (fcc at $T=0$) (meV/Å^2)	74.8 [69]	**55.0**	8.7	26.7	33.9
T_m (K)	933 [66]	925	**940**	926	929
ΔH_m (T_m) (eV/atom)	0.108 [66]	0.100	**0.105**	0.112	0.119
$\Delta V_m / V_{fcc}$ (T_m) (%)	6.5 [66]	8.0	**7.9**	**5.5**	**6.6**
d (liquid at T_m) (atom/Å^3)	0.0528 [67]	**0.0535**	**0.0522**	0.0535	0.0531
B (fcc at T_m) (GPa)		*60*	*48*	58	74
B (liquid at T_m) (GPa)				44	17
$D \cdot 10^5$ (liquid at T_m) (cm^2/s)		3.14	4.58	5.48	5.67
S_2 (eV/(K·atom))		−0.337	−0.294	−0.275	−0.267

Note: [1] The properties used in the fitting procedure are printed in bold. Ercolessi and Adams [30] used slightly different target values. The table does not list all properties used in the fitting procedure in [30]. All properties listed on lines above the melting temperature, T_m, are calculated at $T=0$; a and c are the lattice parameters, E_{coh} is the cohesive energy, $\Delta E_{fcc \rightarrow \alpha}$ is the difference between energies of the α and fcc phases, C_{ij} is the elastic constant, E_f is the point defect formation energy and γ_{ijk} is the free surface energy. All properties listed below T_m are calculated at T_m; ΔH_m and ΔV_m are changes in enthalpy and volume upon melting, d is the liquid density, B is the bulk modulus, D is the diffusivity and S_2 is defined in Equation (7).

Al are fcc metals, the potential should accurately predict that fcc is the most stable phase up to its melting temperature. In the potential development procedure, it is easier to ensure that fcc is the most stable phase at zero temperature, and then to check its melting temperatures relative to those for other possible crystalline lattices. If any other crystalline phase is found to have a higher melting temperature than fcc, the potential necessarily predicts a structural phase transition with increasing temperature below the melting point. Note that such structural transitions are not observed in either Al or Cu, which are known to melt from the fcc phase. The list of target properties in Tables 1 and 2 includes the lattice parameters and the difference in energies between fcc, bcc and hcp phases at zero temperature. The fcc–hcp energy difference is important not only as a check on the low-temperature phase stability, but also due to its relation to the stacking fault energy. Representative crystalline point-defect properties are also included in the target properties of Tables 1 and 2, namely the vacancy and $\langle 100 \rangle$ self-interstitial formation energies.

Tables 1 and 2 also include a number of properties not included in the fitting of the potentials, but which are deemed to be important checks of the potential model.

Table 2. Bulk properties of Cu: target values and values calculated with EAM potentials[1]

Property	Target value	MMPVK	ABCHM	Cu1
a (fcc) (Å)	3.640 [68]	**3.615**	**3.615**	3.639
E_{coh} (fcc) (eV/atom)	−3.540 [63]	**−3.540**	**−3.460**	−3.283
C_{11} (GPa)	170 [64]	**170**	169	175
C_{12} (GPa)	123 [64]	**123**	118	128
C_{44} (GPa)	76 [64]	**76**	71	84
$E_{\mathrm{f}}^{\mathrm{v}}$ (unrelaxed fcc) (eV/atom)	1.074 [68]	**1.309**	1.154	1.065
$E_{\mathrm{f}}^{\mathrm{v}}$ (relaxed fcc) (eV/atom)		1.274	1.122	1.050
$E_{\mathrm{f}}^{\mathrm{m}}$ (fcc) (eV/atom)		0.689	0.904	0.988
E_{D} (fcc) (eV/atom)	2.04 [70]	1.963	2.016	2.038
$E_{\mathrm{f}}^{\mathrm{i}}$ ($\langle 100 \rangle$ fcc) (eV/atom)	2.93 [68]	3.08	3.18	**2.81**
a (bcc) (Å)	2.894 [68]	**2.868**	2.964	**2.895**
$\Delta E_{\mathrm{fcc} \to \mathrm{bcc}}$ (eV/atom)	0.035 [68]	**0.046**	0.024	**0.040**
a (hcp) (Å)	2.561 [68]	**2.556**	2.545	2.569
c (hcp) (Å)	4.232 [68]	**4.162**	4.247	4.211
$\Delta E_{\mathrm{fcc} \to \mathrm{hcp}}$ (eV/atom)	0.007 [68]	**0.008**	0.005	**0.007**
γ ($\langle 100 \rangle$ fcc) (meV/Å^2)	135.2 [69]	84.0	68.0	67.6
γ ($\langle 110 \rangle$ fcc) (meV/Å^2)	139.6 [69]	92.1	73.4	72.0
γ ($\langle 111 \rangle$ fcc) (meV/Å^2)	121.8 [69]	77.4	56.3	56.3
T_{m} (K)	1356 [66]	1326	**1356**	1353
ΔH_{m} (T_{m}) (eV/atom)	0.1347 [66]	0.124	**0.124**	0.142
$\Delta V_{\mathrm{m}}/V_{\mathrm{fcc}}$ (T_{m}) (%)	4.25 [66]	5.02	**3.81**	3.62
d (liquid at T_{m}) (atom/Å^3)	0.0761 [67]	0.0747	**0.0742**	**0.0763**
B (fcc at T_{m}) (GPa)				*119*
B (liquid at T_{m}) (GPa)				
$D \cdot 10^5$ (liquid at T_{m}) (cm^2/s)		2.99	2.51	2.73
S_2 (eV/(K·atom))		−0.313	−0.308	−0.306

Note: [1]The properties used in the fitting procedure are printed in bold. Mishin *et al.* [54] used slightly different target values. The table does not list all properties used in the fitting procedure in [54]. See also the footnote to Table 1.

Such properties include the liquid bulk modulus, liquid diffusivity and zero-temperature surface energies. If the potential is not designed to simulate surface phenomena, the surface energy (γ) may not be a critical property for the potential to reproduce. However, to prevent spontaneous cavitation during MD simulations, the surface energy predicted by the potential should have a reasonable magnitude, and the values of γ predicted for the various potentials considered in this work are, thus, reported in Tables 1 and 2.

2.2. *First-principles calculations of Cu properties*

To augment the database for the fitting of the Cu EAM potential, first-principles calculations were performed to compute the following properties: the structural energy differences between fcc, bcc and hcp structures, the vacancy formation energy and the formation energy of a self interstitial. The calculations were performed using the first-principles electronic-structure code VASP (Vienna *ab initio* simulation package) [33,34], employing Vanderbilt ultrasoft pseudopotentials, the 1991 generalized gradient approximation (GGA) of Perdew and Wang [35,36] and an expansion of the electronic wavefunctions in a plane-wave basis with a kinetic energy cutoff of 350 eV. The Brillouin zone was sampled using the Monkhorst–Pack method [37] with nearly constant k-point densities for each of the different calculations, roughly equivalent to a $12 \times 12 \times 12$ mesh for a conventional fcc unit cell. The electronic states were broadened according to the Methfessel–Paxton scheme [38] with a smearing of 0.1 eV.

The calculated properties for fcc, bcc and hcp Cu structures are given in Table 2; the lattice constants and structural energy differences are in good agreement with previous first-principles calculations employing similar methods [39]. The interstitial formation energy was derived from a $3 \times 3 \times 3$ fcc supercell containing 108 atoms at fcc sites and one extra Cu atom in an interstitial position; for these calculations the energy was fully relaxed with respect to all of the atomic positions within the supercell. For the purposes of the fitting of the potential, it was convenient to use a value for the vacancy formation energy corresponding to 'unrelaxed' geometries; this quantity was computed from the difference in energy between a bulk fcc crystal and a $2 \times 2 \times 2$ fcc supercell containing one vacant site and 31 Cu atoms at ideal fcc lattice positions. The calculated (unrelaxed) vacancy formation energy was found to be smaller than the experimental values reported in [40] (1.27 eV/atom) and in [41] (1.28 eV/atom). Moreover, it is the relaxed vacancy formation energy that should be compared with experimental data, and this quantity is necessarily smaller than the calculated unrelaxed vacancy formation energy, implying an even larger discrepancy with experimental data. However, the first-principles calculations were performed at zero temperature, while the experimental values were obtained at $0.55\,T_\mathrm{m}$ to $0.78\,T_\mathrm{m}$. Therefore, the temperature dependence of the vacancy formation energy should be taken into account when comparing experiment and theory. This point has been discussed previously by Sandberg and Grimvall [42], and we will discuss this issue in further detail in Section 3.2.

2.3. *Diffraction experiments*

To obtain the diffraction data, samples of high purity Al (99.999%) and Cu (99.999%) were sealed in thin-walled 2-mm diameter quartz capillaries and ≈ 67 MPa (≈ 500 Torr) Ar.

The samples were heated uniformly using a cylindrical Pt–Rh wound resistance furnace with a very low temperature gradient [43]. Samples were heated to $\approx 1400\,\mathrm{K}$ before reaction with the container occurred. The HEXRD studies were performed at the MUCAT 6-IDD beamline at the Advanced Photon Source using an energy of $98.9\,\mathrm{keV}$, corresponding to a wavelength (λ) of $0.010029\,\mathrm{nm}$. Silicon double-crystal monochromators were employed to select the wavelength. The diffraction data were collected in transmission using a MAR345(*) image plate detector at a distance around $0.4\,\mathrm{m}$ providing a usable range in the wave momentum number ($Q = 4\pi\sin\Theta/\lambda$) of $\approx 200\,\mathrm{nm}$. The diffracted intensity as a function of Q was obtained by integrating around the Debye rings of the exposed image plate. The wavelength was determined using an energy dispersive detector, while the sample-to-detector distance was determined using NIST Si Standard Reference Material 640C. The required geometric corrections for misalignment of the detector relative to the beam normal were performed using FIT2D [44]. The data were then converted to the total structure function, $S(Q)$, using standard procedures [45,46]. An acquisition time of $200\,\mathrm{s}$ provides high quality data with signal-to-noise comparable to neutron data sets whose acquisition times are one- to two-orders of magnitude longer in duration. The total scattering functions for Al and Cu agree very well with previously published neutron data at similar temperatures [47].

3. Analysis of EAM potentials for Al and Cu

3.1. *EAM potentials for Al*

We started our analysis using the EA potential for Al developed in [30] (the potential parameters were taken from [48]). This potential was fit to a set of crystal properties at room temperature, along with the forces obtained from the first-principles calculations on several model defect and liquid structures. Table 1 shows that the potential provides good agreement with the target properties, with the possible exception of the fcc–hcp and fcc–bcc energy differences, which are nevertheless still very reasonable with this potential. Figure 1 plots the effective pair potential defined as:

$$\varphi^{\mathrm{eff}}(r) = \varphi(r) + 2\frac{\partial\Phi}{\partial\rho}\bigg|_{\rho_0}\psi(r) \tag{4}$$

where ρ_0 is the value of ρ for fcc Al in equilibrium at zero temperature. An interesting feature of the EA model for Al is the presence of two local minima in the attractive part of the potential.

The melting temperature for the EA potential was calculated using the so-called coexistence method [49]. The accuracy of the melting temperature determination is estimated to be not worse than $3\,\mathrm{K}$. As can be seen from Table 1, the EA potential provides good reproduction of the Al melting temperature and the latent heat; however, it predicts a rather large change in volume upon melting. Overall, Table 1 shows that the EA potential provides a good description of solid Al properties and the melting-property data. Surprisingly, this potential predicts a liquid structure that shows clear discrepancies with the experimental data (Figure 2). Specifically, the EA liquid is too strongly ordered, as can be seen from the first peak of the PCF, which is too high relative to experimental measurements. Furthermore, the EA liquid PCF shows some unusual broadening of the second peak, a feature that is more characteristic of a metallic glass
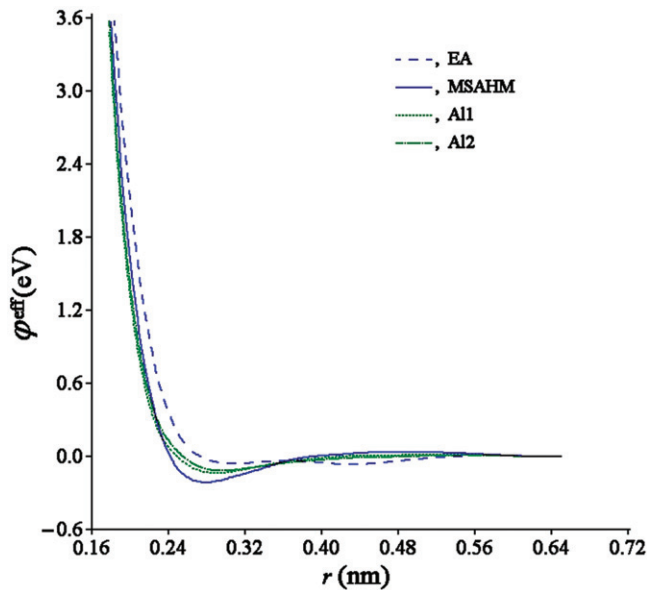
Figure 1. Effective pair potentials calculated from the EAM potentials for Al.

rather than a liquid structure. Moreover, while the EA potential predicts the liquid density and the position of the first peak of the PCF in rather good agreement with experimental data (see Table 1 and Figure 2), it gives a liquid structure factor where the first peak is shifted by 1 1/nm with respect to the experimental first peak position. In addition, the degree of sharpness of the second diffuse scattering peak (Figure 2) of the EA potential, compared to the experimental data, cannot be attributed to any experimental artefact, such as the resolution function, which should have resulted in a more symmetrical deviation from the ideal structure for all peaks.

The second Al potential tested in this work is described in [32], and referred to as the MSAHM potential. It was also fit to zero-temperature crystal properties, melting temperature data and atomic forces obtained from first-principles calculations for a model liquid structure. An analysis of the data in Table 1 shows that the potential provides slightly better agreement with zero-temperature bulk properties than the EA potential, but predicts very low values for surface energies. The poor prediction of the surface energies provided by the MSAHM potential should not be surprising since these quantities were not included in the fitting procedure. Since the number of neighbours of the surface atoms is smaller than those in the bulk, a potential fit to correctly reproduce bulk properties only (including bulk crystal defects) should generally not be expected to correctly reproduce free surface properties. For example, we note that the free surface energy is not correlated with the vacancy formation energy, as can be clearly seen in Table 1. The point is that an atom located near by a vacancy has 11 nearest neighbours, while atoms at a free surface have significantly smaller coordinations. Thus, the region of the embedding energy function, which is important for the calculation of the bulk properties, is distinctly different from the region that is relevant for the atoms at a free surface. It should also be mentioned that the free surface energy is not correlated with the
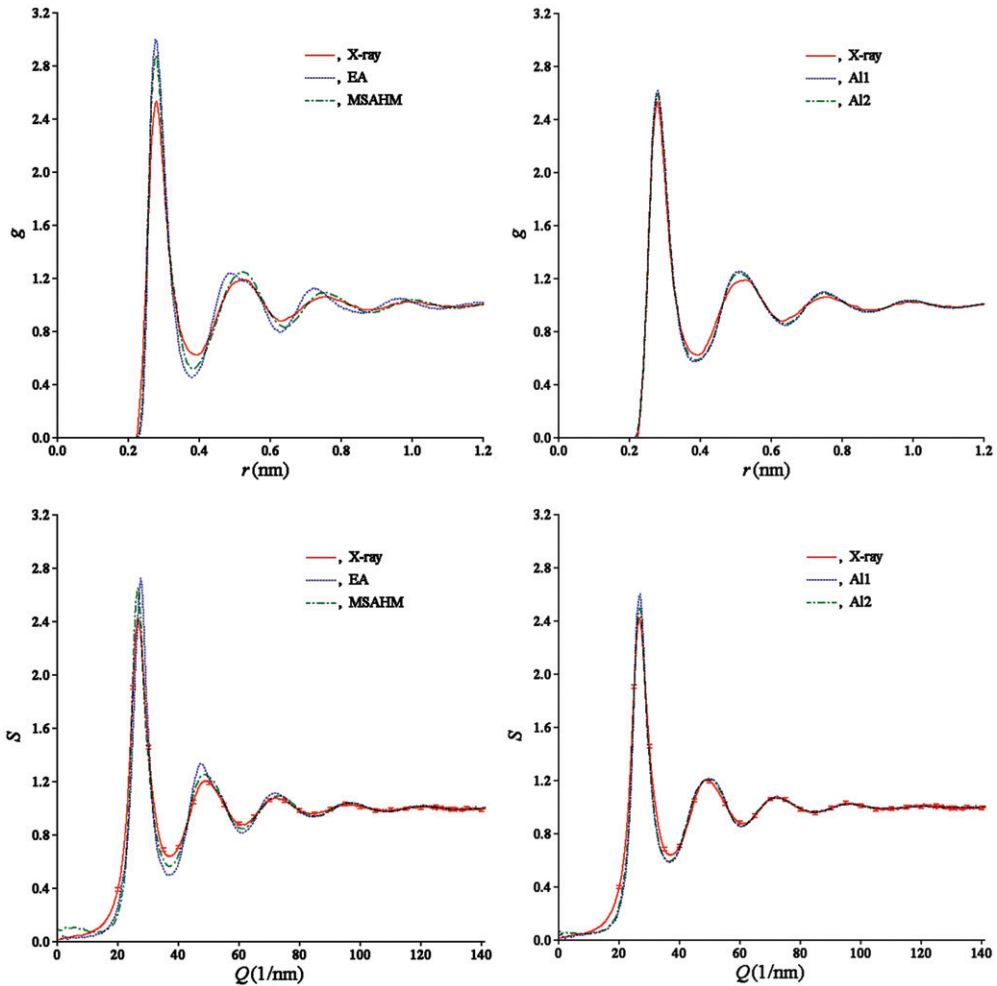
Figure 2. Pair correlation functions and structure factors of liquid Al at $T = 973$ K. All models used to calculate PCFs contained 5000 atoms and were equilibrated during 20 000 MD steps ($\sim$41 ps). PCFs were averaged over the next 20 000 MD steps.

solid–liquid interfacial free energy. For example, it was shown in [28] that the MSAHM potential and another Al potential developed in [27] predict about the same solid–liquid interface free energy, but the potential from [27] predicts values for the surface energies ($\gamma_{100} = 42.4$ meV/Å^2; $\gamma_{110} = 46.1$ meV/Å^2; $\gamma_{111} = 38.5$ meV/Å^2), which are two- to three-times larger than those predicted by the MSAHM potential.

As with the EA potential, the MSAHM potential provides the correct melting temperature and latent heat, but again predicts a relatively large change in volume upon melting. The PCF calculated with this potential (Figure 1) also features a rather high first peak, although it is lower than that obtained with the EA potential despite the fact that the melting temperature is 15 K higher than that for the EA potential. Importantly, the PCF calculated with the MSAHM potential shows no unusual broadening in the second peak;

although this peak is higher than the second peak of the experimental PCF, its position is correctly reproduced.

The analysis presented in Figure 2, as with the results of similar studies [26,50], indicates that the inclusion of atomic forces calculated for model liquid configurations in the potential fitting procedure does not guarantee correct reproduction of the liquid structure. Specifically, it is noteworthy that the EAM potentials predict structures that are more ordered than those suggested by the diffraction experiments. In light of these observations, it is interesting to consider the procedure underlying the force matching method [30]. This method has the distinguishing feature that it allows one to include information about configurations with small atomic separations in the potential development procedure via fitting to the atomic forces obtained from the first-principles calculations on a model liquid structure. The force matching method represents an approach that improves upon earlier strategies, where inclusion of the information about small atomic separations was based on the use of the universal binding energy relation (UBER) [51] to describe the energy for large compressions. Use of the UBER alone leads to potential parameters fit to symmetric atomic configurations, where the density parameter ρ is very large for structures with small interatomic spacings. In contrast, there are low-symmetry atomic configurations with small separations in the liquid where ρ has about the same value as in the equilibrium crystal at zero temperature. Such information is, indeed, important to include in the fitting of the potential to increase its transferability, as found in [26]. However, it should be noted that since the EAM is only an approximate model for metallic bonding, potentials with this form should not be expected to reproduce all first-principles data for thermodynamic and defect properties. Therefore, it is not obvious that forcing an EAM potential to reproduce detailed information, such as the broad distribution of atomic forces in a liquid configuration, might not degrade its accuracy in predictions for other properties.

An alternative way to include the information about small atomic separations in the construction of an EAM potential is to include liquid PCFs directly in the fitting. This method has the advantage that the potential is forced to reproduce the liquid structure only on average. Furthermore, the PCFs can be derived directly from experiment, removing the effect of any systematic errors associated with first-principles calculated forces. The method for including PCFs in the fitting procedure is based on the use of the Born–Green–Bogoliubov (BGB) equation. The procedure was described in detail in [52], and it was successfully applied to the development of an EAM potential for Fe in [26] and Zr in [53].

In the present work, we employed the density function parameterization from the MSAHM potential and refit the pairwise and embedding energy functions using the BGB equation and liquid diffraction data, the zero-temperature crystal properties and melting temperature data. To investigate the sensitivity of the simulation results to the choice of basis functions used to represent the embedding energy, we developed two potentials (Al1 and Al2) with Φ represented by different choices for the basis functions. The parameters of these two potentials are given in Appendix A. Figure 2 demonstrates that the use of the BGB equation in the potential fitting results in an almost perfect agreement with the experimental PCF. As can be seen from Figure 1, the different choice of the basis functions does not lead to considerable differences in the potential shape. An analysis of the results in Table 1 also shows that both potentials provide comparable levels of accuracy in the reproduction of the target properties.

The analysis shown in Figure 1 suggests that the EA potential has the strongest repulsive part. This could explain why this potential provides an overly ordered liquid structure. However, while the repulsive parts of the MSAHM potential and Al1 and Al2 are about the same, the MSAHM potential leads to a much more ordered liquid structure. Obviously, the dependence of the liquid structure on the potential shape is more complex and cannot be correlated in a simple manner with the potential shape.

In relation to the application of interest in this work, namely crystallization kinetics at high undercoolings, it is important to note that even though the different Al potentials considered here predict the same melting point, they will not necessarily predict the same change in free energy upon melting at large supercooling. The difference in free energy between solid and liquid phases can be expressed via the Gibbs–Helmholtz equation as follows:

$$\Delta G_{\mathrm{m}}(T) = T \int_{T}^{T_{\mathrm{m}}} \frac{\Delta H_{\mathrm{m}}}{T^2} \, \mathrm{d}T \tag{5}$$

Equation (5) shows that the change in the free energy depends on the temperature dependence of the latent heat, which can be different for different potentials. As mentioned above, the melting temperature can be accurately obtained from coexistence simulations. It is straightforward to obtain accurate data on the latent heat from MD simulation if both liquid and solid phases do not undergo spontaneous phase transformations at a given temperature. In the cases of the Al EAM potentials considered here, the fcc phase could be overheated up to $1.1\,T_{\mathrm{m}}$, while the liquid phase could be supercooled down to $0.6\,T_{\mathrm{m}}$. Thus, Equation (5) allows us to obtain reliable data on the change in free energy upon melting from $0.6\,T_{\mathrm{m}}$ to $1.1\,T_{\mathrm{m}}$. The data beyond this interval should be viewed as extrapolation.

Figure 3 shows the change in the free energy upon melting calculated via Equation (5). It is clear that at very large supercooling, the EAM potentials considered in the present study give very different predictions for $\Delta G_{\mathrm{m}}(T)$. In particular, the values obtained with the EA and Al2 potential at $T = 400\,\mathrm{K}$ are different by almost a factor of two. As mentioned above, it was found in [28] that the EA potential predicts much higher crystal–melt interfacial free energies than the MSAHM potential. The results in Figure 3 show that the EA potential also predicts rather small bulk thermodynamic driving forces (the change in free energy) for crystallization relative to the MSAHM potential. Thus, it is not surprising that, with the EA potential, crystal nucleation could not be observed on MD time scales during the supercooling of the melt, owing to the relatively large values of the interfacial free energy, combined with the low thermodynamic driving forces.

3.2. *EAM potentials for Cu*

In the case of Cu, we started from potential EAM1 developed in [54], referred to below as MMPVK. The effective pair potential derived from this EAM potential is shown in Figure 4. Analysis of the results in Table 2 shows that the potential provides good agreement with the low-temperature target properties for the crystal, including the self-interstitial formation energy. However, this potential overestimates the first-principles-calculated unrelaxed vacancy formation energy, which is consistent with the
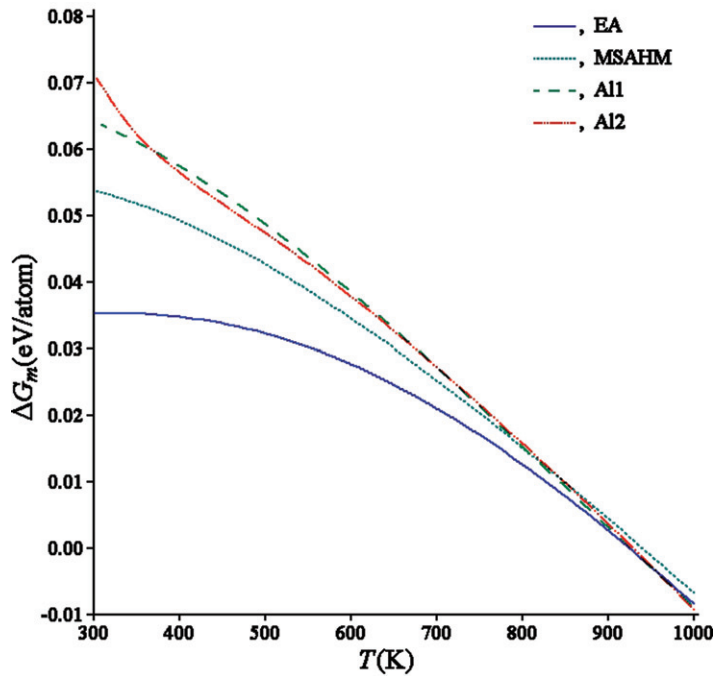
Figure 3. Change in the Gibbs free energy upon melting in Al.
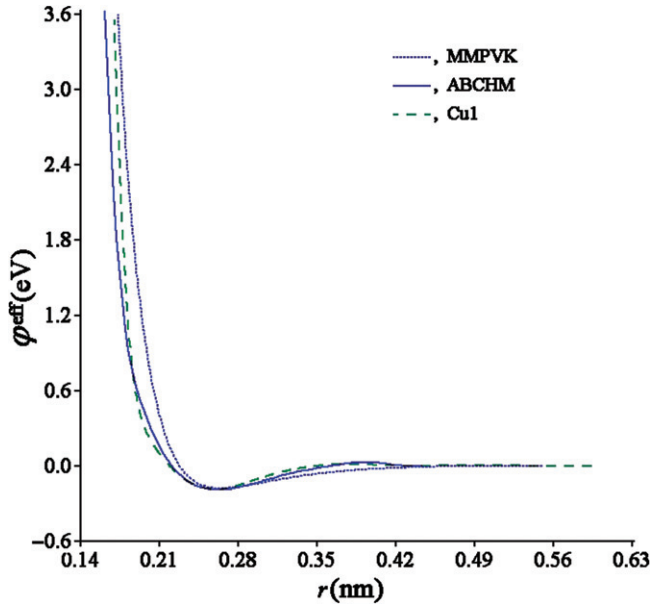

Figure 4. Effective pair potentials calculated from the EAM potentials for Cu.

fact that the authors of [54] used the experimental value of the vacancy formation energy in their fitting procedure. Interestingly, the MMPVK potential predicts a very reasonable melting temperature, even though this property was not included in the fitting procedure. As has been found for most EAM potentials with correct melting temperatures, the MMPVK potential overestimates the height of the first peak of the liquid pair correlation function (see Figure 5), but overall the agreement with the experimental diffraction data for the liquid phase is very reasonable.

Next, we consider the widely used EAM potential for Cu developed in [25], which was fit only to low-temperature crystal properties. We find that the melting temperature for this potential is $T_m = 1494\,\mathrm{K}$, which is 138 K above the actual melting temperature for Cu. To correct this discrepancy, we added one more term in the embedding energy function and refit the pairwise and embedding energy functions (the new potential parameters are given in Appendix A). Table 2 shows the properties calculated with the new potential referred to below as ABCHM. The potential predicts a slightly higher interstitial formation energy and smaller fcc–bcc and fcc–hcp energy differences than obtained from the current first-principles calculations. On the other hand, Figure 5 demonstrates that the ABCHM potential provides very good agreement with the experimental liquid structure data.

Finally, one more Cu EAM potential (referred to below as Cu1) was developed in the present work by fitting to the low-temperature crystal properties, melting temperature data and liquid diffraction data. The analysis of Table 2 and Figure 5 shows that this potential
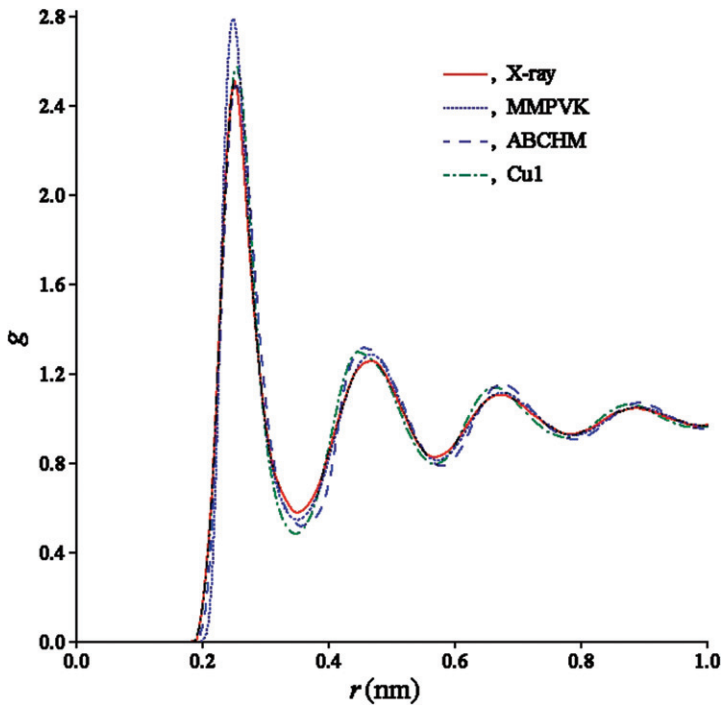

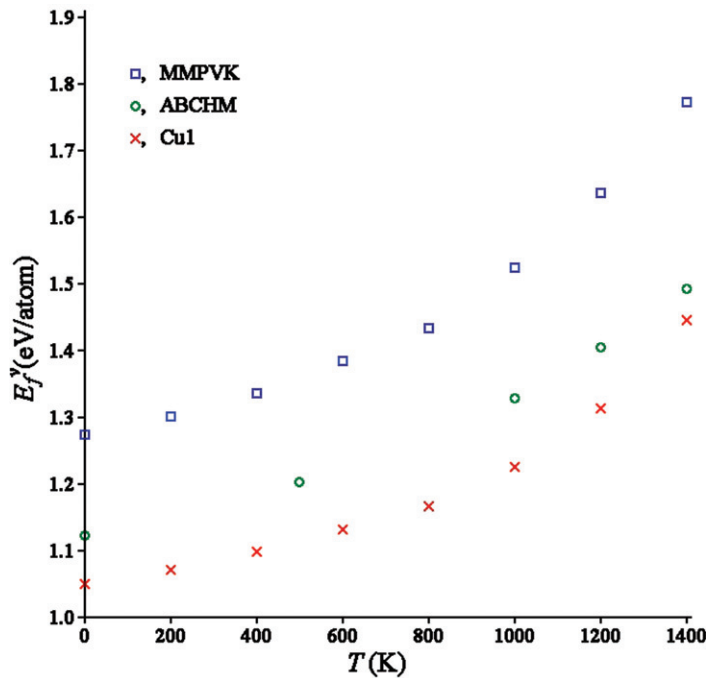Figure 5. Pair correlation functions of liquid Cu at $T = 1373\,\mathrm{K}$.

Figure 6. Vacancy formation energy in Cu as a function of temperature.

provides about the same level of agreement with the target properties as the ABCHM potential, with the exception of the fcc–bcc and fcc–hcp energy differences, which are better reproduced by the potential Cu1. Figure 4 shows that both the ABCHM and Cu1 potentials have a rather similar shape, which nonetheless differs significantly from the MMPVK potential.

As discussed above, we used the value of the unrelaxed vacancy formation energy obtained from our first-principles calculations in the development of the Cu1 potential, and this value seems to be lower than that obtained from experiment. However, our target vacancy formation energy was calculated at zero temperature, while measured vacancy formation energies are usually determined from experiment at $\approx 0.55\,T_m$ to $0.78\,T_m$. To determine how the vacancy formation energy depends on temperature, we performed MD simulations of the perfect fcc lattice containing 2048 atoms and the fcc lattice containing 2047 atoms, with one vacant site, at several temperatures (the temperature dependence of the atomic density was taken into account such that the average pressure in the perfect fcc lattice was always zero). To obtain the vacancy formation energy, the total energy was averaged over 3,000,000 MD steps ($\approx 6\,$ns) in each simulation. The statistical error of such calculations was investigated by performing three independent simulations and is estimated to be less than $0.005\,$eV/atom. The calculated dependencies of the vacancy formation energy on temperature, derived from each of the three Cu EAM potentials considered in this work, are shown in Figure 6. Each of the Cu potentials led to similar predictions for the temperature dependence of the vacancy formation energy, but since each was fit to different values at zero temperature, they predict different results
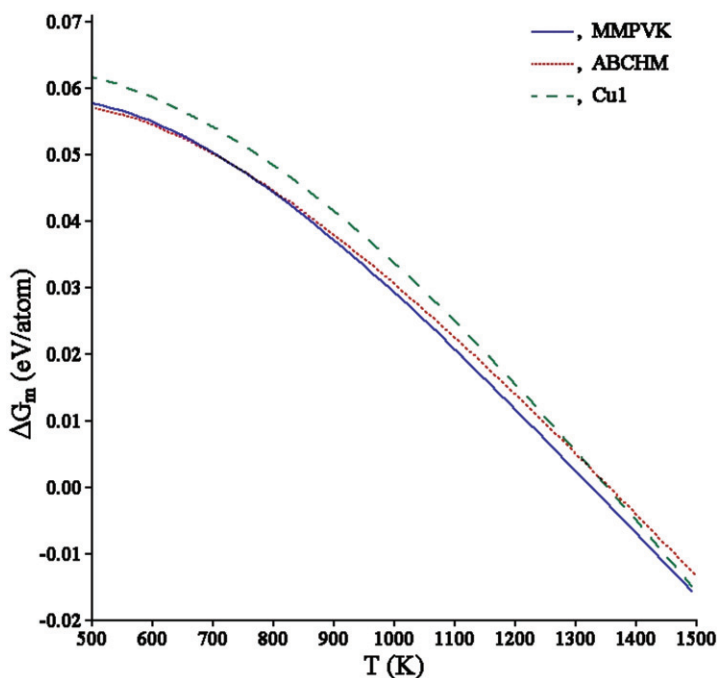
Figure 7. Change in the Gibbs free energy upon melting in Cu.

at $0.8\,T_m$: $1.57\,\mathrm{eV/atom}$ by the MMPVK potential, $1.36\,\mathrm{eV/atom}$ by the ABCHM potential and $1.26\,\mathrm{eV/atom}$ by the Cu1 potential. It is important to note that the Cu1 potential, which reproduced well the first-principles results at zero temperature, also provides the best agreement with the experimental measurements at high temperature. The results obtained here, showing a pronounced effect of the temperature on vacancy formation energy, are consistent with an earlier investigation of the same effect by Sandberg and Grimvall [42]. These authors performed a reanalysis of the high-temperature experimental data accounting for anharmonicity of the atomic vibrations, leading to an estimate of the low-temperature vacancy formation energy of $1.09\,\mathrm{eV}$, in very good agreement with the relaxed values for the ABCHM and Cu1 potentials in Table 2.

Figure 7 plots the calculated change in the free energy upon melting, $\Delta G_m(T)$, as a function of temperature, employing Equation (5) and the method described in the previous section. In contrast to Al potentials, where a dramatic difference between results for $\Delta G_m(T)$ was found using different EAM potentials, all three of the Cu potentials considered here provide very similar predictions from the melting temperature down to $0.4\,T_m$.

4. Determination of liquid diffusivities

All seven of the interatomic potentials (four for Al and three for Cu) described above were used to calculate the liquid diffusivities at the melting temperature. The models

contained 5000 atoms, and 200,000 MD steps (410 ps) were performed. The diffusivities were calculated from the mean-square displacement of the atoms using the following equation:

$$D = \frac{\langle \Delta r^2 \rangle}{6t} \qquad (6)$$

The results of these calculations are given in Tables 1 and 2. An analysis of these results shows that the various EAM potentials produce significantly different values for D. For example, the diffusivity calculated with the Al2 potential is 1.8 times larger than that calculated with the EA potential. The difference between values obtained for Cu is less pronounced (Table 2). In the case of Al, one could suggest that the difference in the diffusivities is related to the difference in liquid structure, as indicated by the calculated PCFs. Indeed, the EA potential predicts the highest first peak of the PCF and, therefore, the more ordered structure. This could be the cause of the lower diffusivity. However, as can be seen from Figure 5, the MMPVK potential also predicts the highest first peak of the PCF amongst the different Cu EAM potentials, but this more strongly ordered liquid structure does not lead to the lowest value of diffusivity.

An alternative way to relate the liquid PCF and diffusivity was proposed in [55], where the diffusion constant, properly scaled, is found to be proportional to the excess entropy of the liquid. The excess entropy can be estimated from the PCF using the following formula:

$$S_2 = -2\pi \frac{N}{V} \int_0^\infty \left\{ g(r) \ln[g(r)] - [g(r) - 1] \right\} r^2 \, \mathrm{d}r \qquad (7)$$

Tables 1 and 2 present values of S_2 calculated for each of the potentials at the melting temperature. The EA potential indeed produces a liquid with the largest excess entropy and, therefore, with the most ordered structure. On the other hand, the value of S_2 for the MMPVK potential is only slightly higher than those calculated for other Cu potentials, a result consistent with the similar values for the diffusivities calculated with each of the different Cu potentials.

5. Molecular dynamics simulation of crystallization kinetics

In this section, we consider the application of MD simulations to the study of crystallization kinetics in highly undercooled melts. We consider, in particular, how results obtained in such simulations are affected by differences in the interatomic potential underlying the simulation. A relatively simple approach to performing such simulations is to consider solidification at constant volume, as in most previous computer simulation studies on vitrification (see, for example, [56]) and recent work on crystal nucleation [20]. However, the approach taken here involves quenching simulations, which begin at some temperature above the melting point and involve relatively rapid cooling rates. For these conditions, crystallization takes place at relatively high undercoolings, where the (negative) pressure in the liquid resulting from a fixed-volume simulation could reach values in excess of 1 GPa. Clearly, such large negative pressures can be

expected to affect crystallization rates and, to avoid this problem, we employed the following method. First, we calculated the equilibrium liquid density at temperatures above $0.6\,T_{\mathrm{m}}$. Then, we determined an interpolation expression for the liquid density to be used in updating the simulation cell volume during cooling. Using this expression, we cooled liquid models containing 5000 atoms, starting at $T_0 = 950\,\mathrm{K}$ for Al and $T_0 = 1400\,\mathrm{K}$ for Cu, to 100 K, with a cooling rate of $2.0 \times 10^{12}\,\mathrm{K/s}$. The temperature and simulation cell volume (using the interpolation expression for the liquid density) were changed after each MD step. Next, we equilibrated the models at zero temperature by relaxing the positions of all the atoms to minimize the total forces acting on each atom, and adjusted cell volume to minimize pressure. This gave us an estimate for the density of the low-temperature glass (for the EA potential, we used a more accurately determined glass density from [31]). We combined the liquid density data and the glass density to obtain new interpolation formulas for the density versus temperature, as given in Appendix B.

Molecular dynamics simulations allow one to cool a system with extremely high rates, which cannot be achieved readily in experiment. For such extreme cooling rates, a system may have no time to reach even metastable equilibrium (see [57] for a more detailed discussion of this issue). On the other hand, simulations at more realistic cooling rates require very long computational time. For the purpose of studying crystallization processes, it is thus important to establish the critical cooling rate, i.e. the fastest cooling rate that can be employed in such a simulation, while still observing crystallization. The critical cooling rate for the MSAHM potential, with a simulation cell containing 5000 atoms, was found to be equal to $3.40 \times 10^{11}\,\mathrm{K/s}$ in [57]. In the present study, we used considerably lower cooling rates of $4.9 \times 10^{10}\,\mathrm{K/s}$ to ensure that the system has sufficient time for nucleation of the solid phase.

In our quenching simulations, all liquids were cooled down to 100 K. The model densities were changed according to the interpolation formula given in Appendix B. The changes of pressure during cooling are plotted in Figures 8 and 9. Examination of these figures shows that five of the seven potentials considered in this work give rise to similar behaviour: the pressure is almost zero until a phase transformation occurs. Figures 10 and 11 plot the energy as a function of temperature during the quench. These plots are similar to those obtained in [14]. These figures support the conclusions made above concerning the observation of a crystallization transition in five of the seven potentials, but the process appears less abrupt on the E versus T plots than on the P versus T plots. Moreover, while some transformation occurs in the simulation using the ABCHM Cu potential around 200 K (Figure 9), no clear signature is seen on the corresponding E versus T curve in Figure 11.

It is interesting to note that the final pressure obtained in the cooling of the liquid described by the EA potential is around 0.9 GPa, even though we used an equilibrium glass density to develop an interpolation formula for the density in performing the quenching simulations for this potential. Moreover, it was found in [31] that the liquid–glass transition in this system has a first-order character, while Figures 8 and 10 do not confirm this conclusion. This is consistent with the results from [58,59], where the authors studied the same potential and did not find any signs of a first-order transition. However, the lowest cooling rate in this previous work was $1.9 \times 10^{12}\,\mathrm{K/s}$, which is higher than in the simulations described above. To clarify the origin of the discrepancy between the conclusions obtained in [31] and [58,59], we performed an additional simulation for the EA
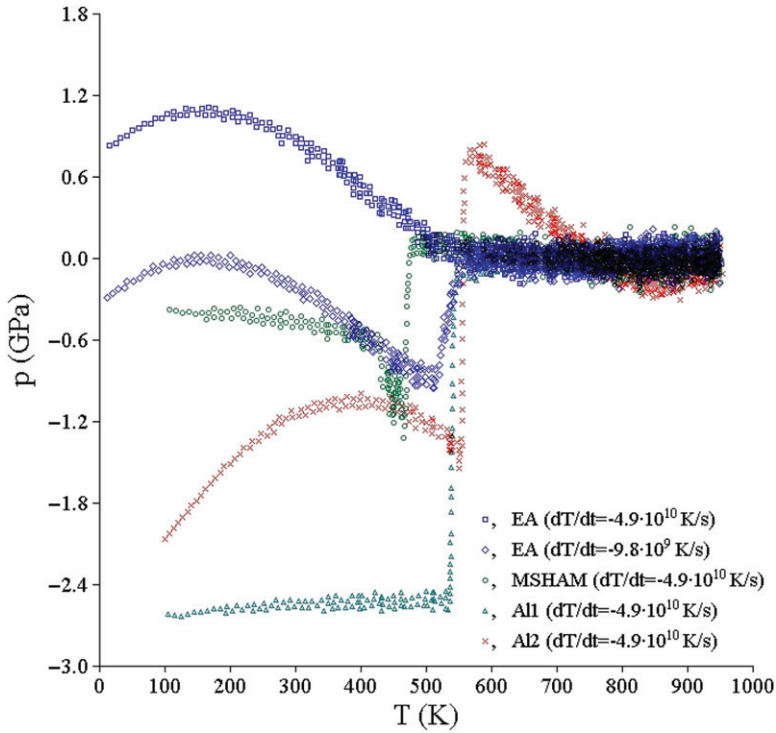
Figure 8. Change of pressure during cooling of Al.

potential using a cooling rate that was lower by a factor of five. As can be seen from Figure 8, with this lower cooling rate, the EA potential shows clear evidence of a first-order phase transformation. However, the latent heat of this transformation is rather small (which is consistent with the data from [31]), such that it is difficult to see indications of this transformation on the E versus T plot (Figure 10).

Thus, we find that all the potentials considered in this work give rise to first-order transformations in quenching simulations, even though these simulations involve relatively short physical time scales. However, it remains to be determined whether the transformations observed in each of the simulations, using different potentials, correspond to crystallization of the stable fcc crystalline phase in each case. To answer this question, we relaxed the final samples resulting from the quenching simulations to zero temperature by relaxing the forces, while keeping the density as predicted by the interpolation formulae discussed above. For each of the resulting structures, we calculated the bond-angle distributions in the first coordination sphere. For all Al models, the radius of this sphere was equal to the position of the first minimum of the liquid PCF obtained using the Al1 potential at $T = 973\,\mathrm{K}$. For all Cu models, we chose a radius for the coordination sphere as determined by the position of the first minimum of the liquid PCF given by the Cu1 potential at $T = 1373\,\mathrm{K}$. Figure 12 shows the bond-angle distribution in the quenched Al models and in perfect fcc and hcp structures. It should be noted that the final structures obtained by the cooling of a liquid using periodic boundary conditions and 5000 atoms
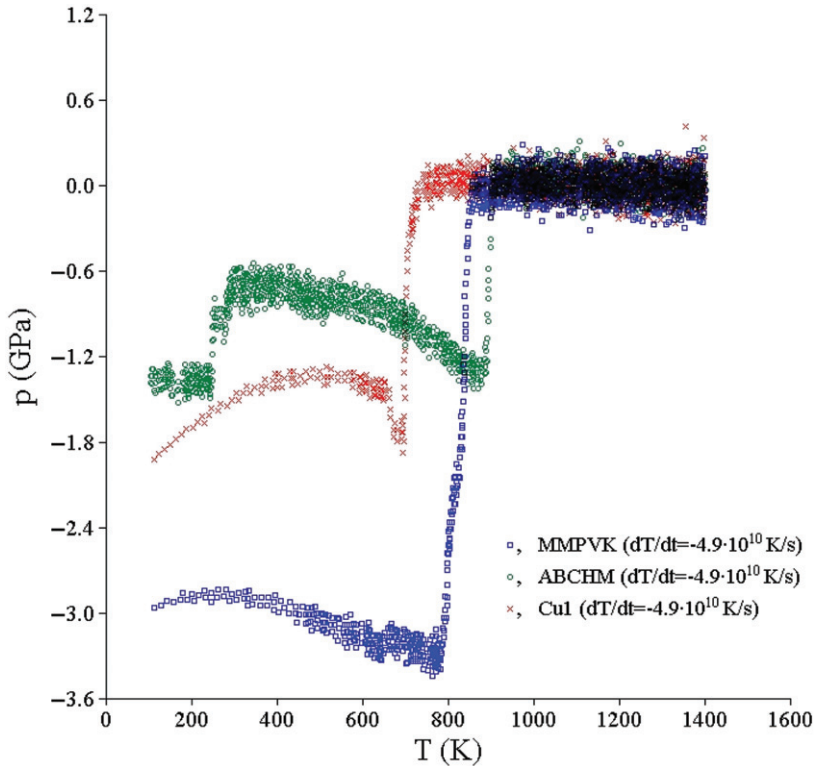
Figure 9. Change of pressure during cooling of Cu.

$(5000 \neq (4i)^{1/3}$, where i is integer) will necessarily contain some defects. Therefore, it should not be expected that the bond-angle distributions in the final models will exactly reproduce those for a perfect fcc lattice. However, the examination of Figure 12 clearly demonstrates that the MSAHM, Al1 and Al2 potentials lead to the formation of the fcc phase during cooling, while the EA potential leads to a more disordered glass structure. Figure 13 shows the bond-angle distributions for the Cu potentials. The examination of this figure shows that the MMPVK or Cu1 potentials both lead to the formation of the fcc phase, while the ABCHM potential leads to formation of a different crystalline structure from the melt during quenching.

6. Discussion and conclusions

In this work, we considered two alternative published EAM potentials for Al (EA and MSAHM) that provide very similar zero-temperature properties for the fcc crystal phase (with the exception of the free surface energies, which are not of direct relevance in the present study) and melting point data. Both potentials were fit to atomic forces obtained on model liquid configurations, computed from first-principles calculations. Nevertheless, the comparison with the experimental diffraction data showed that both
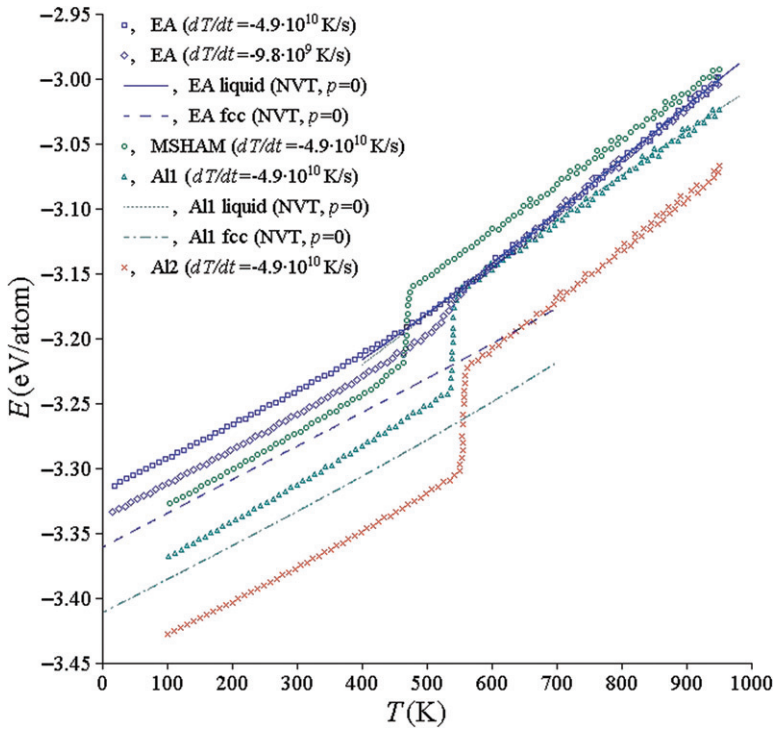
Figure 10.　Change of energy during cooling of Al.

potentials considerably overestimate the height of the first peak of the liquid pair correlation function. One of the potentials (EA) even leads to an unusual broadening of the second peak which is not observed in diffraction experiments on liquid Al. Therefore, we developed two new EAM potentials (Al1 and Al2), the parameters for which were fit to reproduce the experimental PCF along with the zero-temperature crystal properties and melting point data. We found that these two new potentials predict lower absolute values for the excess liquid entropy and considerably higher diffusivities (the diffusivity predicted by the EA potential is more than 1.5 times smaller than the values obtained with the new potentials). Moreover, we found that under larger supercooling, the potentials predict rather different temperature dependencies for the changes in the free energy upon melting. The EA potential, in particular, predicts the smallest absolute values for ΔG_m. Along with the fact that the EA potential predicts a relatively large solid–liquid interface free energy relative to other potentials [28], it is not surprising that crystal nucleation rates under large supercoolings should be very different for the EA relative to other Al potentials. Indeed, we found that while all other Al potentials considered in the present work lead to the crystallization in MD simulation if the cooling rate is sufficiently low, the EA potential leads to vitrification proceeding through a first-order phase transformation. In principle, this phenomenon cannot be considered as being in contradiction with experimental data (in reality, vitrification never has been observed in pure Al) since it still occurs at cooling rates that are so high that they cannot be experimentally achieved. However, it is clear
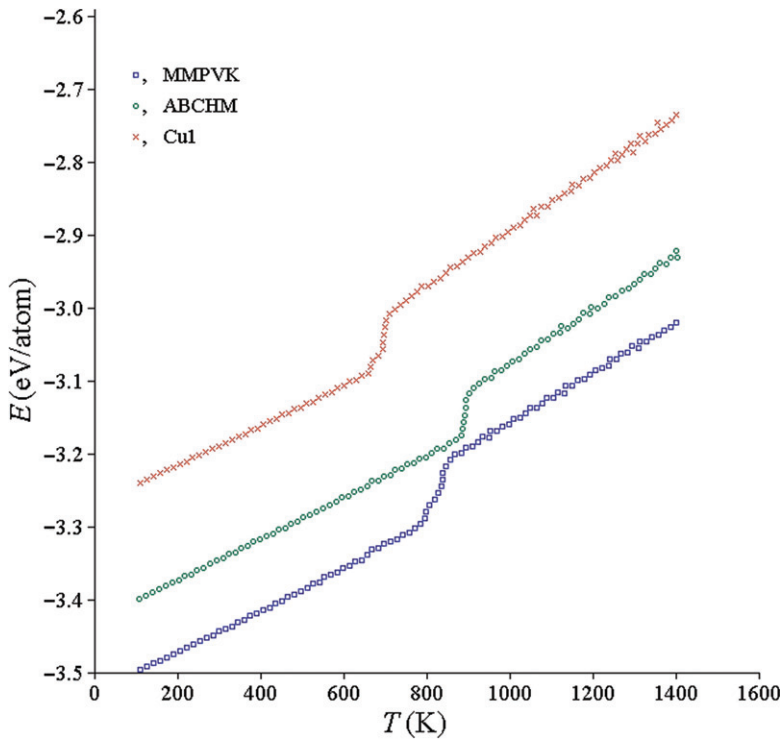
Figure 11. Change of energy during cooling of Cu.

from this study that the different EAM potentials for Al lead to very different kinetics for crystal nucleation, even though they predict very similar low-temperature crystal properties and melting point data.

To investigate whether the observations made in studying crystallization kinetics in Al were specific to that material alone, we also considered EAM potentials for Cu, which also has an equilibrium fcc structure. We considered two EAM potentials (MMPVK and ABCHM) from the literature (the ABCHM potentials was modified to reproduce the melting point data). In comparison with our experimental diffraction data, the MMPVK potential overestimates the height of the first peak of the liquid PCF, but provides excellent agreement with measurements for other peaks. On the other hand, the ABCHM potential provides an excellent prediction for the first peak but worse predictions for the next peaks of the liquid PCF. Both potentials overestimate the vacancy formation energy at zero temperature, in comparison with our first-principles calculations, and at high temperatures, in comparison with experimental measurements. We developed another Cu potential (Cu1) that provides better predictions for the vacancy formation energy and about the same level of agreement with the experimental diffraction data for the liquid structure as the ABCHM potential. All three potentials predict about the same excess liquid entropy and liquid diffusivity. Moreover, all three potentials predict about the same change in the free energy upon melting, even at very
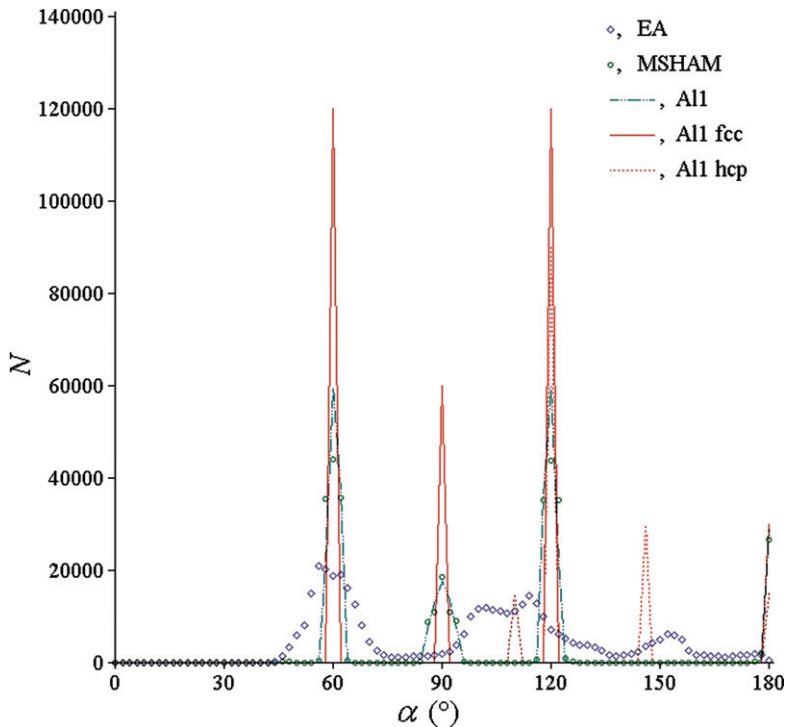
Figure 12. Angle distribution in Al models obtained by cooling from liquid to 100 K and subsequent quenching. The angle distribution for the Al2 potential (not shown here) looks almost identical to that for the Al1 potential.

large supercoolings. Thus, one could expect that these potentials should give rise to very similar kinetics for crystallization from the melt phase. However, our MD simulation showed that, while the MMPVK and Cu1 potentials give rise to the formation of an fcc crystal phase from the melt when the cooling rate is sufficiently low, the ABCHM potential demonstrates more complex behaviour and leads to the formation of another crystal phase.

Our study clearly demonstrates that the results of the MD simulations of crystallization kinetics from highly undercooled melts can be very sensitive to the quality of the underlying semi-empirical potential. The fact that a potential correctly reproduces the crystal properties and even melting point data does not guarantee that it will yield reliable predictions for the liquid properties. We have found that one important test for the quality of the potential is its ability to reproduce experimentally measured liquid structure PCFs. The fast progress in high energy X-ray and neutron diffraction techniques [60,61] will lead to increasing availability of such measurements for testing potential models. However, we have found that, even for potentials where the liquid structure data was included in the potential fitting procedure, it is not guaranteed that the potential will give reliable predictions for the kinetics of the crystallization in highly undercooled melts. Thus, further investigations of how such crystallization kinetics depend on the details of the
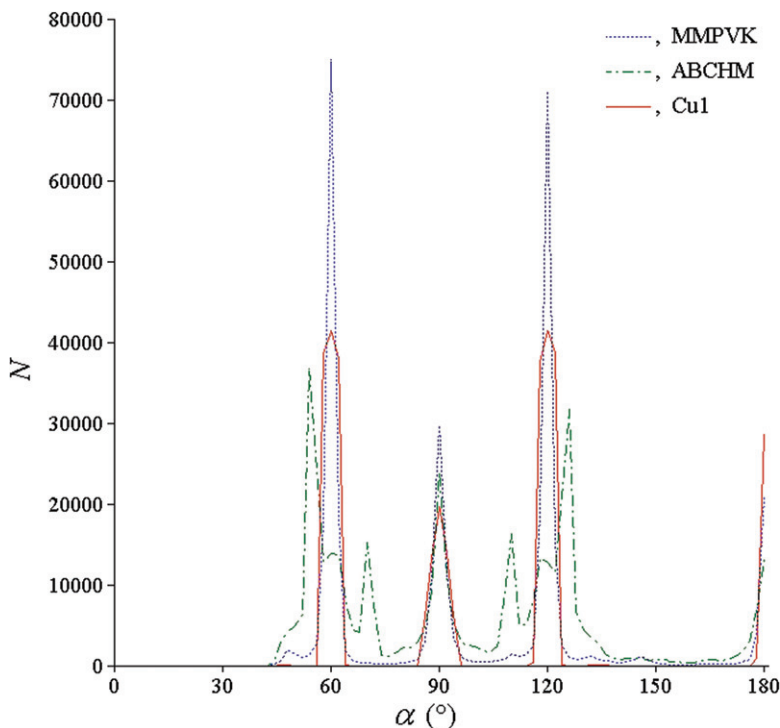
Figure 13. Angle distribution in Cu models obtained by cooling from liquid to 100 K and subsequent quenching.

interatomic interaction are required to more fully understand the range of applicability of semi-empirical potentials in studies of phase transformations under such far-from-equilibrium conditions.

Acknowledgements

References

[1] R.L. Davidchack and B.B. Laird, Phys. Rev. Lett. 85 (2000) p.4751.
[2] R.L. Davidchack and B.B. Laird, J. Chem. Phys. 118 (2003) p.7651.
[3] R.L. Davidchack and B.B. Laird, Phys. Rev. Lett. 94 (2005) p.086102.
[4] J.J. Hoyt, M. Asta and A. Karma, Phys. Rev. Lett. 86 (2001) p.5530.
[5] J.J. Hoyt and M. Asta, Phys. Rev. B 65 (2002) p.214106.
[6] J.J. Hoyt, M. Asta and A. Karma, Mater. Sci. Eng. A 41 (2003) p.121.
[7] J.R. Morris and X.Y. Song, J. Chem. Phys. 119 (2003) p.3920.
[8] D.Y. Sun, M. Asta, J.J. Hoyt et al., Phys. Rev. B 69 (2004) p.020102(R).
[9] J.Q. Broughton, G.H. Gilmer and K.A. Jackson, Phys. Rev Lett. 49 (1982) p.1496.
[10] F.C. Celestini and J.-M. Debierre, Phys. Rev. B 62 (2000) p.14006.
[11] J.J. Hoyt, B. Sadigh, M. Asta et al., Acta Mater. 47 (1999) p.3181.
[12] D.Y. Sun, M. Asta and J.J. Hoyt, Phys. Rev. B 69 (2004) p.174103.
[13] F. Celestini and J.M. Debierre, Phys. Rev. E 65 (2002) p.041605.
[14] H.W. Sheng, J.H. He and E. Ma, Phys. Rev. B 65 (2002) p.184203.
[15] S. Kazanc, Comput. Mater. Sci. 38 (2006) p.405.
[16] J. Wedekind, D. Reguera and R. Strey, J. Chem. Phys. 125 (2006) p.214505.
[17] L. Wang, C. Peng, Y. Wang et al., J. Phys.: Condens. Matter 18 (2006) p.7559.
[18] J. Liu, J.Z. Zhao and Z.Q. Hu, Appl. Phys. Lett. 89 (2006) p.031903.
[19] L. Wang, C. Peng, Y. Wang et al., Phys. Lett. A 350 (2006) p.69.
[20] R.S. Aga, J.R. Morris, J.J. Hoyt et al., Phys. Rev. Lett. 96 (2006) p.245701.
[21] M.W. Finnis and J.E. Sinclair, Phil. Mag. A 50 (1984) p.45.
[22] M.S. Daw and M.I. Baskes, Phys. Rev. B 29 (1984) p.6443.
[23] S.M. Foiles, M.I. Baskes and M.S. Daw, Phys. Rev. B 33 (1986) p.7983.
[24] M. Igarashi, M. Khantha and V. Vitek, Phil. Mag. B 63 (1991) p.603.
[25] G.J. Ackland, D.J. Bacon, A.F. Calder et al., Phil. Mag. A 75 (1997) p.713.
[26] M.I. Mendelev, S. Han, D.J. Srolovitz et al., Phil. Mag. 83 (2003) p.3977.
[27] J.B. Sturgeon and B.B. Laird, Phys. Rev. B 62 (2000) p.14720.
[28] Morris J.R., Mendelev M.I. and Srolovitz D.J., J. Non-Cryst. Solids (2008), in press.
[29] Y. Waseda, *The Structure of Non-crystalline Materials*, McGraw-Hill, New York, 1980.
[30] F. Ercolessi and J.B. Adams, Europhys. Lett. 26 (1994) p.583.
[31] M.I. Mendelev, J. Schmalian, C.Z. Wang et al., Phys. Rev. B 74 (2006) p.104206.
[32] M.I. Mendelev, D.J. Srolovitz, G.J. Ackland et al., J. Mater. Res. 20 (2005) p.208.
[33] G. Kresse and J. Hafner, Phys. Rev. B 47 (1993) p.558.
[34] G. Kresse and J. Hafner, J. Phys.: Condens. Matter 6 (1994) p.8245.
[35] J.P. Perdew, in *Electronic Structure of Solids '91*, P. Ziesche and H. Eschrig eds., Akademie Verlag, Berlin, 1991, p.11.
[36] J.P. Perdew, J.A. Chevary, S.H. Vosko et al., Phys. Rev. B 46 (1992) p.6671.
[37] H.J. Monkhorst and J.D. Pack, Phys. Rev. B 13 (1976) p.5188.
[38] M. Methfessel and A.T. Paxton, Phys. Rev. B 40 (1989) p.3616.
[39] Y. Wang, S. Curtarolo, C. Jiang et al., Comput. Coupl. Phase Diag. Thermochem. 28 (2004) p.79.
[40] W. Balluffi, J. Nucl. Mater. 69/70 (1978) p.240.
[41] R.W. Siegel, J. Nucl. Mater. 69/70 (1978) p.117.
[42] N. Sandberg and G. Grimvall, Phys. Rev. B 63 (2001) p.184109.
[43] L. Margulies, M.J. Kramer, R.W. McCallum et al., Rev. Sci. Instrum. 70 (1999) p.3554.
[44] A.P. Hammersley, S.O. Svensson, M. Hanfland et al., High Press. Res. 14 (1996) p.235.
[45] Y. Waseda and M. Ohtani, Phys. Status Solidi B 62 (1974) p.535.
[46] T. Egami and S.J.L. Billinge, *Underneath the Bragg Peaks: Structural Analysis of Complex Materials*, Elsevier, Amsterdam, 2003, p.404.

[47] O.J. Eder, E. Erdpresser, B. Kunsch et al., J. Phys. F: Metal Phys. 10 (1980) p.183.
[48] X.-Y. Liu, P.P. Ohotnicky, J.B. Adams et al., Surf. Sci. 373 (1997) p.357.
[49] J.R. Morris, C.Z. Wang, K.M. Ho et al., Phys. Rev. B 49 (1994) p.3109.
[50] D.Y. Sun, M.I. Mendelev, C.A. Becker et al., Phys. Rev. B 73 (2006) p.024116.
[51] J.H. Rose, J.R. Smith, F. Guinea et al., Phys. Rev. B 29 (1984) p.2963.
[52] M.I. Mendelev and D.J. Srolovitz, Phys. Rev. B 66 (2002) p.014205.
[53] M.I. Mendelev and G.J. Ackland, Phil. Mag. Lett. 87 (2007) p.349.
[54] Y. Mishin, M.J. Mehl, D.A. Papaconstantopoulos et al., Phys. Rev. B 63 (2001) p.224106.
[55] M. Dzugutov, Nature 381 (1996) p.137.
[56] S. Sastry, P.G. Debenedetti and F.H. Stillinger, Nature 393 (1998) p.554.
[57] M.I. Mendelev, R.S. Aga, J.R. Morris et al., (2008), in preparation.
[58] C.S. Liu, Z.G. Zhu, J. Xia et al., J. Phys.: Condens. Matter 13 (2001) p.1873.
[59] G.X. Li, Y.F. Liang, Z.G. Zhu et al., J. Phys.: Condens. Matter 15 (2003) p.2259.
[60] A.K. Gangopadhyay, G.W. Lee, K.F. Kelton et al., Rev. Sci. Instrum. 76 (2005) p.073901.
[61] D. Holland-Moritz, T. Schenk, P. Convert et al., Meas. Sci. Technol. 16 (2005) p.372.
[62] The first-principles calculations were performed by G.J. Ackland. The details can be found in [32].
[63] C. Kittel, *Introduction to Solid State Physics*, Wiley, New York, 1986.
[64] W.B. Pearson, *A handbook of lattice spacings and structures of metals*, Pergamon, Oxford, 1967.
[65] N. Sandberg, B. Magyari-Köpe and T.R. Mattsson, Phys. Rev. Lett. 89 (2002) p.065901.
[66] C.I. Smithels, *Metals Reference Book*, Butterworths, London, 1976.
[67] P.P.Arsentev, *Metallicheskie rasplavy i ikh svoistva* (Metallurgia, Moscow, 1976) (in Russian).
[68] First principle calculations performed as part of this work.
[69] L. Vitos, A.V. Ruban, H.L. Skriver et al., Surf. Sci. 411 (1998) p.186.
[70] P.G. Shewmon, *Diffusion in Solids*, McGraw-Hill, New York, 1963.

Appendix A: EAM potential functions developed in the present work

All1: Function	Value	Cutoffs
$\varphi(r)$	$\exp(0.65196946237834 + 7.6046051582736 \cdot r - 5.8187505542843 \cdot r^2 + 1.0326940511805 \cdot r^3)$	1.5–2.3
	$+13.695567100510(3.2 - r)^4$	2.3–3.2
	$-44.514029786506(3.2 - r)^5$	2.3–3.2
	$+95.853674731436(3.2 - r)^6$	2.3–3.2
	$-83.744769235189(3.2 - r)^7$	2.3–3.2
	$+29.906639687889(3.2 - r)^8$	2.3–3.2
	$-2.3612121457801(4.8 - r)^4$	2.3–4.8
	$+2.5279092055084(4.8 - r)^5$	2.3–4.8
	$-3.3656803584012(4.8 - r)^6$	2.3–4.8
	$+0.94831589893263(4.8 - r)^7$	2.3–4.8
	$-0.20965407907747(4.8 - r)^8$	2.3–4.8
	$+0.24809459274509(6.5 - r)^4$	2.3–6.5
	$-0.54072248340384(6.5 - r)^5$	2.3–6.5
	$+0.46579408228733(6.5 - r)^6$	2.3–6.5
	$-0.18481649031556(6.5 - r)^7$	2.3–6.5
	$+0.028257788274378(6.5 - r)^8$	2.3–6.5

Al1:

Function	Value	Cutoffs
$\psi(r)$	$0.00019850823042883(2.5 - r)^4$	0–2.5
	$+0.10046665347629(2.6 - r)^4$	0–2.6
	$+0.10054338881951(2.7 - r)^4$	0–2.7
	$+0.099104582963213(2.8 - r)^4$	0–2.8
	$+0.090086286376778(3.0 - r)^4$	0–3.0
	$+0.0073022698419468(3.4 - r)^4$	0–3.4
	$+0.014583614223199(4.2 - r)^4$	0–4.2
	$-0.0010327381407070(4.8 - r)^4$	0–4.8
	$+0.0073219994475288(5.6 - r)^4$	0–5.6
	$+0.0095726042919017(6.5 - r)^4$	0–6.5
$\Phi(\rho)$	$-\rho^{1/2}$	0–∞
	$-6.1596236428225 \cdot 10^{-5}(\rho - 16)^4$	16–∞
	$+1.4856817073764 \cdot 10^{-5}\,(\rho - 16)^5$	16–∞
	$-1.4585661621587 \cdot 10^{-6}(\rho - 16)^6$	16–∞
	$+7.2242013524147 \cdot 10^{-8}(\rho - 16)^7$	16–∞
	$-1.7925388537626 \cdot 10^{-9}(\rho - 16)^8$	16–∞
	$+1.7720686711226 \cdot 10^{-11}(\rho - 16)^9$	

Al2:

Function	Value	Cutoffs
$\varphi(r)$	$\exp(1.0655898030717 + 6.9189333025554 \cdot r - 5.4560152009179 \cdot r^2 + 0.97305935423516 \cdot r^3)$	1.6–2.25
	$+10.797831008871(3.2 - r)^4$	2.25–3.2
	$-38.354420072333(3.2 - r)^5$	2.25–3.2
	$+83.609733168086(3.2 - r)^6$	2.25–3.2
	$-75.644960845874(3.2 - r)^7$	2.25–3.2
	$+27.397628449176(3.2 - r)^8$	2.25–3.2
	$-1.6404275277304(4.8 - r)^4$	2.25–4.8
	$+1.9359384900534(4.8 - r)^5$	2.25–4.8
	$-2.3676607051992(4.8 - r)^6$	2.25–4.8
	$+0.68948838258734(4.8 - r)^7$	2.25–4.8
	$-0.14749445109681(4.8 - r)^8$	2.25–4.8
	$+0.19214771321964(6.5 - r)^4$	2.25–6.5
	$-0.40788777117632(6.5 - r)^5$	2.25–6.5
	$+0.33795215935241(6.5 - r)^6$	2.25–6.5
	$-0.12880925102229(6.5 - r)^7$	2.25–6.5
	$+0.019019373704492(6.5 - r)^8$	2.25–6.5
$\psi(r)$	The same as for Al1	
$\Phi(\rho)$	$-\rho^{1/2}$	0–∞
	$+3.5025051308271 \cdot 10^{-4}(\rho - 16)^4$	16–∞
	$-6.9606881126760 \cdot 10^{-5}(\rho - 16)^5$	16–∞
	$+3.5717262505601 \cdot 10^{-6}(\rho - 16)^6$	16–∞
	$-1.8828783364689 \cdot 10^{-3}(\rho - 24)^4$	24–∞
	$+1.1303817967915 \cdot 10^{-6}(\rho - 24)^5$	24–∞
	$-8.0158124278034 \cdot 10^{-6}(\rho - 24)^6$	24–∞
	$+2.7235851330782 \cdot 10^{-4}(\rho - 30)^4$	30–∞
	$+4.8914043715808 \cdot 10^{-5}(\rho - 30)^5$	30–∞
	$+4.7226737586655 \cdot 10^{-6}(\rho - 30)^6$	30–∞

ABCHM: Function	Value	Cutoffs
$\varphi(r)$	$\exp(0.81808226148375 + 16.009784353249 \cdot r - 15.726771924462 \cdot r^2 + 3.8001997136343 \cdot r^3)$	1–1.9
	$+0.61727034877621(4.4274528135 - r)^3$	1.9–4.4274528135
	$-3.0176798528760(4.174260021 - r)^3$	1.9–4.174260021
	$+2.8363729125862(4.0415934975 - r)^3$	1.9–4.0415934975
	$-0.40972326434610(3.615 - r)^3$	1.9–3.615
	$+0.64644167838571(3.130681821 - r)^3$	1.9–3.130681821
	$+0.81340753490858(2.556191082 - r)^3$	1.9–2.556191082
$\psi(r)$	$0.2075858369(4.4274528135 - r)^3$	0–4.4274528135
	$+0.3550816685(3.615 - r)^3$	0–3.615
$\Phi(\rho)$	$-\rho^{1/2} + 1.5746965651016 \cdot 10^{-5} \rho^2$	0–∞

Cu1: Function	Value	Cutoffs
$\varphi(r)$	$\exp(11.026565103477 - 10.167211017722 \cdot r + 6.0017702915006 \cdot r^2 - 1.9598299733506 \cdot r^3$	1–1.8
	$+3.3519281301971(2.8 - r)^4$	1.8–2.8
	$-47.447602323833(2.8 - r)^5$	1.8–2.8
	$+111.06454537813(2.8 - r)^6$	1.8–2.8
	$-122.56379390195(2.8 - r)^7$	1.8–2.8
	$+49.145722026502(2.8 - r)^8$	1.8–2.8
	$+4.0605833179061(4.8 - r)^4$	1.8–4.8
	$+2.5958091214976(4.8 - r)^5$	1.8–4.8
	$+5.5656640545299(4.8 - r)^6$	1.8–4.8
	$+1.5184323060743(4.8 - r)^7$	1.8–4.8
	$+0.39696001635415(4.8 - r)^8$	1.8–4.8
	$-0.21402913758299(6.0 - r)^4$	1.8–6.0
	$+1.1714811538458(6.0 - r)^5$	1.8–6.0
	$-1.9913969426765(6.0 - r)^6$	1.8–6.0
	$+1.3862043035438(6.0 - r)^7$	1.8–6.0
	$-0.34520315264743(6.0 - r)^8$	1.8–6.0
$\psi(r)$	$0.019999999875362(2.4 - r)^4$	0–2.4
	$+0.019987533420669(3.2 - r)^4$	0–3.2
	$+0.018861676713565(4.5 - r)^4$	0–4.5
	$+0.0066082982694659(6.0 - r)^4$	0–6.0
$\Phi(\rho)$	$-\rho^{1/2}$	0–∞
	$-5.7112865649408 \cdot 10^{-5}(\rho - 9)^4$	9–∞
	$+3.0303487333648 \cdot 10^{-4}(\rho - 11)^4$	11–∞
	$-5.4720795296134 \cdot 10^{-4}(\rho - 13)^4$	13–∞
	$+4.6278681464721 \cdot 10^{-4}(\rho - 15)^4$	15–∞
	$-1.0310712451906 \cdot 10^{-3}(\rho - 16)^4$	16–∞
	$+3.0634000239833 \cdot 10^{-3}(\rho - 16.5)^4$	16.5–∞
	$-2.8308102136994 \cdot 10^{-3}(\rho - 17)^4$	17–∞
	$+6.4044567482688 \cdot 10^{-4}(\rho - 18)^4$	18–∞

Note: The potential functions are available in a tabulated format at http://www.ctcms.nist.gov/potentials

Appendix B. The interpolation formulae $V(T)$ used to supercool liquids[1]

Potential	Interpolation formula
EA	$16.499273654685 + 1.4069118357962 \cdot 10^{-4}\,T + 2.9910138575409 \cdot 10^{-6}\,T^2 - 6.5039828854356 \cdot 10^{-10}\,T^3$
MSAHM	$16.950544068828 + 8.3784462149119 \cdot 10^{-4}\,T + 1.2676335153420 \cdot 10^{-6}\,T^2 + 3.9958330569841 \cdot 10^{-10}\,T^3$
Al1	$17.382037069004 + 6.4020953782951 \cdot 10^{-4}\,T + 1.0171605320429 \cdot 10^{-6}\,T^2 - 2.0304034049849 \cdot 10^{-10}\,T^3$
Al2	$17.421186061216 - 1.1181702649231 \cdot 10^{-3}\,T + 2.8767491111760 \cdot 10^{-6}\,T^2$
MMPVK	$12.121109014543 + 3.8554706486947 \cdot 10^{-4}\,T + 6.3234830062039 \cdot 10^{-7}\,T^2 - 1.5197787531933 \cdot 10^{-10}\,T^3$
ABCHM	$12.693461852769 + 1.0533485872603 \cdot 10^{-4}\,T + 3.5241993934760 \cdot 10^{-7}\,T^2$
Cu1	$12.384609494237 - 1.1551782948521 \cdot 10^{-5}\,T + 4.5038939033397 \cdot 10^{-7}\,T^2 - 3.3289420460390 \cdot 10^{-11} * T^3$

Note: [1]Atomic volume is expressed in the units of Å^3/atom.